

**COMPARING FAN BEAM AND CONE BEAM CT FOR NON-CLINICAL IMAGING
OF TUBERCULOSIS**

by

Michelle Sutphin

A Thesis

Submitted to the

Graduate Faculty

of

George Mason University

in Partial Fulfillment of

The Requirements for the Degree

of

Master of Science

Biology

Committee:

Dr. Ancha Baranova,
Committee Chair

Dr. Laura Via, Thesis Director and
Committee Member

Dr. Vikas Chandhoke,
Committee Member

Dr. Iosif Vaisman, Director,
School of Systems Biology

Dr. Donna M. Fox, Associate
Dean, Office of Student Affairs &
Special Programs, College of Science

Dr. Peggy Agouris, Dean,
College of Science

Date: _____ Spring Semester 2019
George Mason University,
Fairfax, VA

Comparing Fan Beam and Cone Beam CT for Non-Clinical Imaging of Tuberculosis

A Thesis submitted in partial fulfillment of the requirements for the degree of Master of Science at George Mason University

by

Michelle Sutphin
Licensed Veterinary Technician
Penn Foster, 2015
Bachelor of Science
Palm Beach Atlantic University, 2003

Director: Laura Via, Thesis Director
George Mason University

Spring Semester 2019
George Mason University
Fairfax, VA

Copyright 2019 Michelle Sutphin
All Rights Reserved

DEDICATION

This is dedicated to my loving husband Joe, my wonderful daughter Victoria, and my family.

ACKNOWLEDGEMENTS

I would like to thank the many friends, relatives, and supporters who have made this happen. My loving husband, Joe, and daughter, Victoria, helped me push through the tough times by never letting me give up. Drs. Via, Gomez Buitrago, and the other members of the Tuberculosis Imaging Program were of invaluable help. Finally, thanks go out to the Mercer Library for providing a clean, quiet, and well-equipped repository in which to work.

TABLE OF CONTENTS

| | |
|--|------------|
| List of | |
| Tables..... | vii |
| List of Figures..... | viii |
| List of Equations..... | ix |
| List of Abbreviations and Symbols..... | x |
| Abstract..... | xi |
| Introduction..... | 1 |
| 1.1: Computed Tomography..... | 1 |
| 1.2: Cone Beam Computed Tomography vs Fan Beam Computed Tomography | 3 |
| 1.3: Non-Clinical Use of FBCT and CBCT | 4 |
| 1.4: Determining a Houndfield Unit (HU)..... | 6 |
| Materials and Methods..... | 7 |
| 2.1: FBCT vs CBCT Protocols | 7 |
| 2.2: Defining a Houndfield Unit (HU) | 8 |
| 2.3: Animals and Ethics Assurance | 11 |
| 2.4: Bacterial Culture, Infection, and Clinical Endpoint Monitoring of Rhesus Macauques | 11 |
| 2.5: Calibration methods on a FBCT and CBCT using a low contrast phantom | 12 |
| 2.6: CT Scanning Procedures | 12 |
| 2.7: CT Data Analysis | 13 |
| 2.8: Statistical Analysis..... | 14 |
| Results | 15 |

| | |
|--|-----------|
| 3.1: Performance of the FBCT and CBCT scanner using a low contrast phantom | 15 |
| 3.2: Results of the acquisition settings for both the FBCT and CBCT | 16 |
| 3.3: Artifacts in the scan of free breathing macaque adversely affects the total lung volume available for whole lung analysis | 16 |
| 3.4: Density difference in the normal lung vs diseased lung were detectable on the CBCT | 19 |
| 3.5: Quantification comparison of tubercular disease as captured by a CBCT and FBCT..... | 20 |
| 3.6: Identifying disease over time between a FBCT and CBCT | 23 |
| 3.7: Single lesion identification on FBCT using established HU ranges..... | 24 |
| 3.8: Single lesion identification on CBCT using established HU ranges..... | 26 |
| 3.9: Disease progression comparison between FBCT and CBCT on one rhesus macaque..... | 28 |
| 3.10 Changes in disease volume over time on a CBCT vs FBCT | 29 |
| Discussion | 32 |
| Conclusion | 37 |
| Appendix | 38 |
| References..... | 40 |

List of Tables

| | |
|---|----|
| Table 1 Acquisition modes for naïve and infected non-human primates..... | 7 |
| Table 2 Low contrast phantom mean values and standard deviation of CT numbers (HU) | 16 |
| Table 3 Acquisition settings for the FBCT and CBCT | 17 |

List of Figures

| | |
|---|----|
| Figure 1 Hounsfield unit scale..... | 11 |
| Figure 2 A breath hold is necessary to collect a lung image for quantitative analysis | 19 |
| Figure 3 Representative images of normal lung and diseased lung as captured by the two scanners | 21 |
| Figure 4 Normal and diseased lung profiles from images collected on the FBCT and CBCT | 24 |
| Figure 5 Visualizing changes in disease over time | 26 |
| Figure 6 Single lesion identification on a FBCT using established HU range..... | 27 |
| Figure 7 Single lesion identification on a CBCT using established HU range..... | 29 |
| Figure 8 Disease progression/regression over 10 weeks on a FBCT and CBCT | 31 |
| Figure 9 Change in disease volume over time on a FBCT vs CBCT | 33 |

List of Equations

| | |
|-------------------------|---|
| Computed CT number..... | 9 |
|-------------------------|---|

List of Abbreviations and Symbols

| | |
|-------------|--|
| CBCT | Cone beam computed tomography |
| CT | computed tomography |
| DICOM | Digital imaging and communications in medicine |
| FBCT | Fan beam computed tomography |
| FOV | Field of view |
| HU | Hounsfield unit |
| kVp | Peak kilovoltage |
| mA | milliamperage |
| MIP | Maximum intensity projection |
| MRI | Magnetic resonance imaging |
| MTb..... | Mycobacterium tuberculosis |
| NHP | Non-human primate |
| OWP | Old-world primate |
| PET | Positron-emission tomography |
| ROI | Region of interest |
| SPECT | Single-photon emission computed tomography |
| TB | Tuberculosis |
| uA | microampерage |
| WLA | Whole lung analysis |

ABSTRACT

COMPARING FAN BEAM AND CONE BEAM CT FOR NON-CLINICAL IMAGING OF TUBERCULOSIS

Michelle Sutphin, M.S.

George Mason University, 2019

Thesis Director: Dr. Laura Via

Objective: To determine the hounsfield unit (HU) range of normal lung tissue and tubercular diseased lung tissue of the same rhesus macaque on repeat scans using two different manufacturers' scanners, a non-clinical cone beam computerized tomography scanner (CBCT) versus a clinical fan beam computerized tomography scanner (FBCT).

Methods: Serial CT scans on two different CT imaging systems was performed on three rhesus macaques (*Macaca mulatta*) prior to and after infection with *Mycobacterium tuberculosis* (*Mtb*). A low-tube-voltage protocol of 80kV, 820uA at 90ms exposure time/projection (Mediso) and a previously optimized high-tube-voltage protocol consisting of 120kV, 5mA (CereTom) were compared. Tissue composition parameters were analyzed in hounsfield units (HU). Differences between protocols on the cone beam CT and the fan beam CT series were documented.

Results: Thoracic CT's of the same three macaques were scanned serially on both machines every two weeks starting 4 weeks post bronchial installation of Mtb. Including a breath hold in the scanning methodology is necessary to prevent liver artifacts and motion which can obscure TB granulomas, as well as, decrease the total lung volume. These artifacts interfere with the assessment of the HU values of the overall lung. The geometry by which each scanner works is disparate, and the HU range obtained on the FBCT appears to show tubercular lesions as denser than the CBCT. The non-clinical CBCT generated smaller voxels which significantly improved spatial resolution as compared to the FBCT. However, the FBCT generated smaller voxels over a wider slice thickness which increased the voxel size to capture more photons which in turn generated images with less noise and more sensitive to HU density changes.

Conclusion: FBCT and CBCT scanner identified diseased lung at approximately the same HU density range, starting around -500 HU and decreasing to a negligible value around +200 HU in monitoring the disease of a *M. tuberculosis* infected rhesus macaque.

Keywords: Fan beam CT, cone beam CT, Hounsfield unit, Mycobacterium tuberculosis, rhesus macaque, computed tomography

INTRODUCTION

Molecular imaging is defined as the visual representation, characterization, and quantification of biological processes at the cellular and subcellular levels within intact living organisms; this can be achieved by various imaging technologies such as nuclear imaging (PET or SPECT), optical imaging (microscopy), magnetic resonance imaging (MRI), ultrasound imaging, and/or computed tomography (CT)¹.

SPECT and PET scans are primarily used to diagnose and track the progression of a disease using radiopharmaceutical activity within an organ². CT and MRI scans are able to produce detailed cross-section images of the body. CT uses computerized x-rays (ionizing radiation), while MRI employs the combination of powerful magnets and radio waves capable of imaging without the use of radiation³. These imaging modalities are particularly attractive because they allow serial measurements in a single subject at many time points during disease progression or treatment.

1.1 Computed Tomography

Computed tomography (CT) was made possible through the work of several individuals, most notably Godfrey Newbold Hounsfield and Allan MacLeod Cormack. For their work, Hounsfield and Cormack shared the 1979 Nobel Prize in Medicine and Physiology. CT uses x-rays transmitted through the patient and to special detectors that convert the radiation beam into digital data for processing by a computer. The computer

uses sophisticated algorithms called image reconstruction techniques to build up and display images of a patient's internal anatomy for diagnostic interpretation. These cross-sectional images are planar sections, or slices, that are perpendicular to the long axis of the patient⁴.

The technology used in CT has evolved from scanning a single slice to multiple slices (multi-slice scanner) in a single breath-hold. Current state-of-the-art CT systems are based on volume data acquisition, in which the x-ray tube and detectors rotate continuously around the patient to gather transmission data from a volume of tissue rather than from 1 slice at a time. Volume-based technology expanded CT use to sophisticated applications in diagnostic CT imaging, along with nuclear medicine and radiation therapy. CT equipment and software are by their very nature complex, and entire textbooks are devoted to describing the technology and algorithms in detail⁴.

In addition, CT imaging now forms the basis for radiation treatment planning, also known as CT simulation⁵. Most CT simulators include a CT scanner with a flat patient table (unlike the curved table of a diagnostic CT scanner), laser beams to aid in patient positioning, and software for virtual simulation. CT simulation aid radiation therapy planning and delivery by accurate defining and localizing tumor in a given patient.

The increasing use of CT has led to widespread concern about relatively high doses of irradiation received by patients undergoing CT examinations as compared to other radiography examinations. In accordance to the as low as reasonably achievable (ALARA) principle, efforts have focused on how to reduce CT irradiation doses. Subsequently, a

number of innovative tools have been developed by CT manufacturers, such as automatic exposure control (tube current modulation); automatic voltage selection (x-ray spectra optimization); efficient x-ray beam collimation; improved x-ray detectors; and more recently image reconstruction techniques based on iterative reconstruction algorithms⁶.

1.2 Cone Beam Computed Tomography vs Fan Beam Computed Tomography

Cone beam CT (CBCT) is a recent technology. Imaging is accomplished by using a cone shaped X-ray beam with a single or partial 360° scan where the X-ray source and a reciprocating array of detectors simultaneously move around the patient. Single projection images, known as “basis” images, are acquired at certain degree intervals. The series of basis projection images is referred to as the projection data, on which software algorithms are applied to generate a 3D volumetric data set, which can be used to provide primary reconstruction images in all three orthogonal planes (axial, sagittal, and coronal). This procedure varies from a traditional medical CT, which uses a fan-shaped x-ray beam in a helical progression to acquire individual image slices of the FOV and then stacks the slices to obtain a 3D representation (Supplementary Image 1). Each slice requires a separate scan and separate 2D reconstruction. Because CBCT exposure incorporates the entire FOV, only one rotational sequence of the gantry is necessary to acquire enough data for image reconstruction⁷.

The cone-beam geometry was developed as an alternative to conventional CT using either fan-beam or spiral-scan geometries, to provide more rapid acquisition of a data set

of the entire FOV and it uses a comparatively less expensive radiation detector. Obvious advantages of such a system, which provides a shorter examination time, include an increase in image sharpness, caused by the translation of the patient, reduced image distortion due to internal patient movements, and increased x-ray tube efficiency⁷.

The CBCT still exhibits many weaknesses that can affect image quality. Current CBCT acquisition modes are aimed at minimizing dose to the patient. This reduction in dose may prove to be beneficial to the patient, but it may reduce the quality of the images and the accuracy of the assigned hounsfield unit (HU). Compounding this issue is the intrinsic problem that the large cone geometry produces more artifacts and scatter than the conventional fan beam CT (FBCT)⁸. With this knowledge in mind, it may prove beneficial to objectively compare the image quality and dose delivered by CBCT and FBCT. This comparison can be accomplished by changing acquisition parameters, analyzing the quality of reconstructed images after defining the features necessary for image quality, and examining absorbed dose statistics that will take subjective bias out of the equation⁹.

1.3 Non-Clinical Use of FBCT and CBCT

In July 2010, the research branch of European Association of Nuclear Medicine (EANM), Research 4 Life (EARL), set up the FDG-PET/CT accreditation program, to help imaging sites meet the standard requirements indicated in the EANM guidelines. In North America, the Society of Nuclear Medicine and Molecular Imaging started the Clinical Trials Network (CTN) to help facilitate the effective use of molecular imaging radiopharmaceuticals in clinical trials¹⁰. There are to date, no organizations or guidelines

for optimization, standardization, acquisition and interpretation of non-clinical PET/CT imaging. Identifying and establishing the hounsfield unit (HU) ranges for organs of interest and tubercular diseased tissue for both the cone beam and fan beam CT for our rhesus colony will provide species specific guidelines not only for the rhesus macaque, but also for other species used as models of tuberculosis infection, such as the common marmoset (*Callithrix jacchus*) and New Zealand White rabbit (*Oryctolagus cuniculus*) often imaged with the fan beam CT.

Comparative studies of animal anatomy have traditionally relied on detailed dissections to produce anatomical illustrations. Recently, an advent of modern imaging modalities, such as MRI and CT, had been developed to represent an enormous resource that allows for fast non-invasive visualization of anatomy in living animals ¹¹. In particular, 3D computer modelling provides morphological and anatomical information in a minimal-invasive and fast way ¹². While both PET and CT have been already utilized extensively to describe human anatomy, this approach is still uncommon in the realm of biomedical research, especially in studies performed on rhesus macaques, common marmosets and rabbits.

Old-world primates are naturally susceptible to *M. tuberculosis* and exhibit all aspects of the human disease including non-necrotic and necrotic primary and secondary granulomas, caseation, cavitation, latency and reactivation ¹³. The NHP model provides the opportunity to characterize disease processes that more closely resemble human TB than the more commonly used mouse TB models ^{14,15}. Following the disease progression from

baseline to 10 weeks post infection will allow us to profile *M. tuberculosis* infection through quantitative HU values.

1.4 Defining a Hounsfield Unit (HU)

A hounsfield unit (HU) scale is a scale of tissue density and is based off 3 values: air -1000HU (minimum HU value), water 0HU and bone +1000HU. Density of all other tissues is falls within this range, usually from -1000 to +1000HU. The purpose of this thesis is to determine the HU unit range of normal lung tissue and tubercular diseased lung tissue in the same rhesus macaque on repeat scans done on two different manufacturers' scanners, a cone beam CT (Mediso) versus a fan beam CT (CereTom). Documentation of the HU range on both scanners will help set the baseline values for the rhesus macaque. These techniques will be important for future studies on this and other species who lack guidelines such as the common marmoset and New Zealand white rabbits.

MATERIALS AND METHODS

2.1 FBCT and CBCT Protocols

Standard imaging protocols for the CBCT and FBCT were generated to investigate the differences in HU profile in diseased and normal lung tissue of the rhesus macaque on these scanners. In this study, all FBCT scans were performed with a NeuroLogica CereTom (NeuroLogica, Inc., MA, USA) which was manufactured to be used as a mobile clinical head scanner. The scanning parameters for the FBCT: 120kVp, 5mA, 1.25mm slice thickness, axial FOV of 150mm, and longitudinal FOV of 260mm, 0.49mm X 0.49mm pixel size and a 512X512 pixel matrix. Furthermore, for the cone beam CT, a Mediso LFER150 (Mediso, Budapest, Hungary) utilized the following parameters: 80kVp, 820uA, 0.5mm slice thickness, axial FOV of 150mm, and a pixel size of 0.5mm X 0.5mm. (see Table 1).

Table 1: Acquisition modes for naïve and infected rhesus macaques

Acquisition modes and parameters for CBCT and FBCT scans for naïve and infected rhesus macaque protocols for this study.

| Scanner | kVp | Amperage | FOV | Scan Type |
|---------|-----|----------|--------|-----------|
| FBCT | 120 | 5 mA | 150 mm | helical |
| CBCT | 80 | 820 uA | 150 mm | axial |

The dose length product (DLP) is fourteen times higher than that of the CBCT. These displayed numbers are really machine output metrics of radiation and not patient specific doses. The CTDI is calculated from a weighted average of the peripheral doses and center line dose that is delivered to a 32cm homogenous plastic phantom for adults and 16cm diameter plastic phantom for pediatric patients. When a patient is CT scanned, the CTDI represents the weighted average dose that either the 32cm or 16cm phantom would have received if the that phantom was scanned with the same radiographic parameters as the patient. The displayed DLP is calculated from the product of the scan length and the weighted average of dose to the phantom, if the phantom has been scanned at those parameters. It represents the total radiation energy deposited in the patient's body. This is an indirect approximation, under multiple slice conditions and is not to be referred to as a dose. These two metrics along with other factors can be used to calculate the effective dose to the patient ¹⁶.

2.2 Defining a Hounsfield unit (HU)

Each CT imaging slice consists of a matrix of voxels (number of voxels across the slice), the FBCT makes a 512 x 512 matrix and the CBCT consist of a 416 x 416 matrix (Supplementary Image 2). During the scanning phase, the individual rays of the x-ray beam are projected through the patient's body. They are attenuated (absorbed) in proportion to the attenuation properties of the tissue along the path. Because of the characteristics of the x-ray beam used in CT (high KV and heavy filtration) the attenuation is highly dependent on tissue density with more dense tissues absorbing more of the x-rays that pass through

them. This property is represented by the value of the attenuation coefficient for the specific tissue.

CT image reconstruction is a mathematical process for converting the scan data (MIP) into a digital image (DICOM) of a specific anatomical area. Our images are created with either the filtered back-projection method (FBP) or sometimes with an enhanced process known as an iterative reconstruction. During the reconstruction process the attenuation coefficient value of each individual voxel is calculated. However, we never see the actual attenuation coefficient values because there is another step in the mathematical process performed by the computer. We will not discuss this mathematical process in this paper.

A CT number value is calculated from the attenuation coefficient value for each voxel and becomes the value for the corresponding pixel in the digital image. A pixel is defined as a two-dimensional picture element that makes up the matrix. Each pixel represents a CT number and is the building block of the matrix and image. The CT number is also known as the hounsfield unit (HU). Water is used as the reference and calibration material for CT numbers. Water has the assigned CT number value of zero. Tissues or other substances that are denser than water will have positive (+) values and those that are less dense will have negative (-) values with air being assigned a HU value of -1000. CT numbers are computed using the following algebraic expression:

$$\text{CT Number} = \frac{\mu_{\text{Tissue}} - \mu_{\text{Water}}}{\mu_{\text{Water}}} \times K$$

where K is the scaling factor (contrast factor) of the CT manufacturer. In general, K is equal to 1000. The range of CT numbers produced using this factor is referred to as the

Hounsfield (H) scale, which results in 0.1% per CT number, thus expressing linear attenuation coefficients much more accurately compared with the scale used in pioneering CT units ⁴.

A voxel is defined as a three-dimensional element of anatomy represented by the two-dimensional pixel. The voxel volume = pixel height x pixel width x slice thickness. The HU is a volume-less unit that is directly related to the density of the material the x-rays are traveling through. Each voxel is given a number based on how much of the x-rays reach the detector. A material with a positive HU value absorbed more x-rays and is denser than water, such as bone (+1000 HU). A material with a negative HU value allowed more x-rays to pass through and reach the detector making it less dense than water, such as air (-1000 HU).

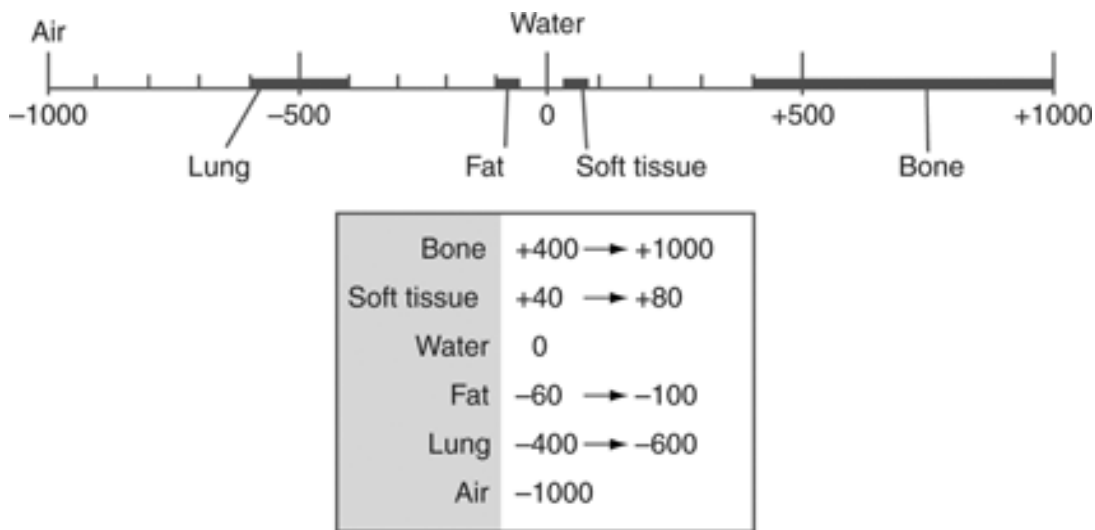


Figure 1 Hounsfield unit scale, diagram courtesy Cambridge University Press.

2.3 Animals and ethics assurance.

This study was carried out in accordance with the recommendations in the Guide for the Care and Use of Laboratory Animals of the National Institutes of Health. The Committee on the Ethics of Animal Experiments of the National Institute of Allergy and Infectious Disease approved the experiments described here under protocol LPD-25E and all efforts were made to provide intellectual and physical enrichment for the rhesus macaques and minimize their suffering. One month prior to infection, macaques were housed individually in biocontainment cages in an animal biological safety level 3 (ABSL3) facility approved for the containment of *M. tuberculosis*.

2.4 Bacterial culture, infection, and clinical endpoint monitoring of rhesus macaques.

Frozen *M. tuberculosis* H37Rv stock cultures tagged with the fluorescent protein mCherry were diluted to ~50 CFU in 2mL. Within a dedicated ABSL3 laboratory, sedated macaques were placed in right lateral recumbency and using a mouth gag to keep the jaw open, 25CFU of *M. tuberculosis* was instilled using a bronchoscope (PENTAX Medical, Japan) navigated to the macaque's right lower lung lobe. The bronchoscope was flushed with 10mL of saline. After infection, the animals were observed daily and given extra nutritional enrichment once a day. Animals were monitored daily for signs that they were becoming clinically ill, as assessed by a combination of weight loss and/or any signs of disease. Potential signs included physical and behavioral changes due to disease, such as tachypnea, dyspnea, or lethargy.

2.5 Calibration methods on a FBCT and CBCT using a low contrast phantom.

A low contrast phantom, similar to a Catphan® phantom, was used to determine the performance of the FBCT and CBCT. A Catphan® phantom is used for quality control of CT scanners to evaluate image quality and detect calibration decay of the scanner.

2.6 CT scanning procedures.

Animals were anesthetized using glycopyrrolate (0.01 mg/kg of body weight intramuscularly [IM]) followed by ketamine (10 mg/kg of body weight IM) and dexmedetomidine (0.03 mg/kg of body weight IM). The animals were then intubated using a laryngoscope (Welch Allyn) and either a 3.0 or 3.5 french endotracheal tube, depending upon the animal's size. A 22-gauge intravenous catheter (IVC) was placed prior to scanning in either the left or right cephalic vein. Normal saline was started intravenously at 10 ml/kg/hr. During scanning, the animals were kept in the appropriate anesthetic plane with a 1 to 3% isoflurane delivery rate via the endotracheal tube. The macaques were attached to a ventilator (Model 2002, Hallowell, Pittsfield, MA) which mechanically ventilated the animals throughout the entire procedure. The breaths per minute (BPM) were determined by the patient's weight and disease level. A button was depressed and held for the duration of the 41 s breath hold during the CT collection. All mechanical ventilation was suppressed. When the button was released, the ventilator returned to the pre-set mechanical state. The breath hold was held during the expiratory phase of the respiratory cycle. A 250-mm FBCT scan from the base of the skull spanning the lungs and the abdominal cavity was acquired in approximately 25 s using an 8-slice helical CT scanner

(CereTom; NeuroLogica, Danvers, MA) using the following parameters: 120 kV, 5 mA/s, 1.25-mm slice thickness, and 0.49x49-mm pixel spacing. A 150mm CBCT scan from the base of the skull spanning the lungs and cranial abdominal cavity was acquired in approximately 41 s using a semi-circular single FOV CBCT scanner (LFER150; Mediso, Budapest, Hungary) using the following parameters: 80 kVp, 980 uA/ s, 0.5-mm slice thickness and 0.5x0.5-mm pixel spacing.

2.7 CT data analysis.

A whole lung analysis was performed by importing the post processed FBCT DICOM (Digital Imaging and Communications in Medicine) files into MIM (MIM Encore™, version 6.8.2, Cleveland, OH) a nuclear medicine fusion software. The CT image was viewed in the lung window followed by performing the “region grow” function to identify the normal lung tissue in the range of -500 to -1024 HU. Once outlined, a slice-by-slice analysis is performed to eliminate the esophagus, descending vena cava, large vessels, and liver. General knowledge of anatomy is used to locate these organs. The chest wall, heart, and large vessels were separated from the lung by tracing the natural contour of the chest wall, heart, and large vessels. Dense lesion centers were subsequently identified for inclusion in the lung region manually to create the 3D region of interest (ROI) for analysis. The remaining area within the lung’s ROI was then analyzed using MIM which generated a histogram of the HU of each voxel within the ROI.

ROI for individual rhesus and rabbit lung density and volume were defined by isolating the lungs using the CT and whole lung analysis (WLA). The volume of disease

was calculated by summing the binned disease from -500 to +200 HU. Next, the sum from each week was subtracted from baseline to show the change in disease volume and % voxel from the non-diseased tissue of baseline. This process was continued for each week on both scanners.

2.8 Statistical analysis:

Curves of the percentage of voxels over a range of HU values were generated in MIM from lung ROI's of naïve and infected macaques. The total volume of disease, in milliliters, was calculated using the binned percentage of voxels multiplied by the total volume of the right lung. The graphs were generated in GraphPad Prism 8.0 and compared to determine the shifts of HU density within the lung ROI's over time, and the advancement of tubercular disease.

RESULTS

3.1 Performance of the FBCT and CBCT scanner using a low contrast phantom

A low contrast phantom, similar to ones used to calibrate clinical scanners, was scanned in each scanner to capture the complete characterization of maximum imaging performance for the FBCT and CBCT. The HU values for the CBCT and the FBCT show an obvious discrepancy because of the beam types (Table 2). This commanded a need to identify and establish new HU density ranges for normal and diseased tubercular tissues for scans collected on the CBCT.

Table 2: Low contrast phantom, mean values and standard deviations of CT numbers (HU). The PMP plastic may not have been made to the NEMA standard because of the discrepancy on both scanners. The FBCT HU values for the various other materials were similar to the standards, but the CBCT showed a negative shift in HU for LDPE, Acrylic and Delrin toward the lower density range (see figure 1) suggesting that the CBCT scanner's report of the tissues falling in those density ranges would be much different than in our previously published work with the FBCT.

| | NEMA Standards | FBCT Mean HU | FBCT σ HU | CBCT Mean HU | CBCT σ HU |
|---------|----------------|--------------|------------------|--------------|------------------|
| Air | -1000 | -1000 | 9 | -994 | 12 |
| PMP | -200 | 69 | 18 | -10 | 42 |
| LDPE | -100 | -106 | 18 | -183 | 39 |
| Acrylic | 120 | 79 | 19 | 20 | 40 |
| Delrin | 340 | 328 | 20 | 265 | 43 |
| Teflon | 990 | 1006 | 19 | 946 | 55 |

3.2 Results of the acquisition settings for both the FBCT and CBCT

The values seen in Table 3 are the direct result of the scanner parameter settings outlined in Table 1. These values fluctuate as the parameters are modified. The DLP volume was 14 times higher in the clinical FBCT than the non-clinical CBCT. This is due to the higher energy (kVp and mA) generated by the FBCT.

Table 3. Acquisition settings for the FBCT and CBCT. They will vary based off of the x-ray tube settings and FOV.

| Scanner | Voxel Size | Image Dimension | DLP |
|----------------|-----------------------|------------------------|------------------|
| FBCT | 0.49 x 0.49 x 1.25 mm | 512 x 512 x 190 | 368.375 mGy x cm |
| CBCT | 0.5 x 0.5 x 0.5 mm | 416 x 416 x 302 | 27.4 mGy x cm |

3.3 Artifacts in the scan of a free breathing macaque adversely affect the total lung volume available for whole lung analysis.

Artifacts can seriously degrade the quality of CT images to the point of being diagnostically unusable. To optimize image quality, artifacts need to be minimized as much as possible. While artifacts are generated from a variety of sources, figure 2 shows how a physical artifact, movement of the liver and diaphragm, interferes with a thoracic cavity

analysis. When the patient free breaths, a percentage of the lung volume is obscured by these anatomical artifacts making identifying tiny nodules incredibly difficult.

Requesting a patient to hold their breath is a universal practice when imaging the thoracic cavity. In non-clinical imaging, this is accomplished by anesthetizing and ventilating the subject to achieve the same static affect. Small nodules can form anywhere within the pulmonary space and can arise from a variety of conditions (cancer, infectious disease, environmental conditions, etc.). They often start off very small and can progress quickly into larger lesions and masses. The settings of the CT scanner including, focal spot size, detector element size, collimation, pitch, slice thickness, increment, reconstruction algorithm and kernel (filters), matrix size, and the reconstruction FOV determine nodules <1mm in size can be identified¹⁷.

In figure 2, the breath hold was captured and the coronal view (figure 2A) and transaxial view (2B) lung mask is traced in blue. The histogram (figure 2C) identifies the majority of voxels fall between -900 and -500 HU. This is the typical HU range for normal lung tissue of an inflated rhesus macaque lung on the FBCT. The height and width of this peak is determined by the inflation volume.

In Figure 2D, the red arrow marks the liver artifact. As DG3P breaths freely during the scan, the liver enters the field of view twice. The lung volume difference between the breath hold and free breathing image was measured, and the free breathing image decreased in volume by 14%. Our typical analysis is based off of volume and a breath hold is necessary to help standardize total lung volume and minimize movement to reduce blurring of small pulmonary nodules for precise analysis.

In the transaxial view, Figure 2E, a slight hazy/fuzziness can be seen on the left side of the image marked by the red arrow. This is a diaphragmatic artifact, indicating movement of the diaphragm, or breathing. The diaphragmatic artifact distorts the image making TB lesions extremely hard to impossible to identify. The liver density captured in the lung ROI gives the impression of dense lung volume when it is only soft tissue in the lung ROI.

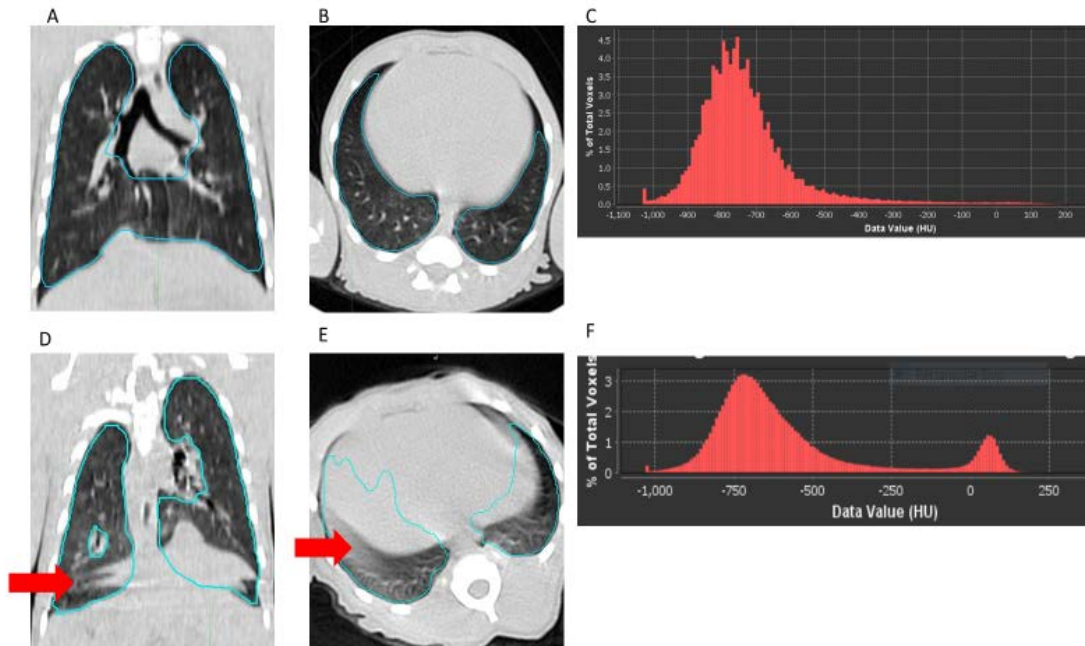


Figure 2 A breath hold is necessary to collect a lung image for quantitative analysis

Coronal, transaxial and histogram images (plates A-C). (A) A naïve rhesus macaque image captured during a 25 second breath hold. The lung has been outlined (blue) and there is no artifact or distortion from the liver or diaphragm. (C) The histogram has one defined curve (-950 to -400 HU) indicating most HU values are closer to air (-1000 HU). The same naïve rhesus macaque 26 days prior free breathing during CT (plates D-F). The lung has been outlined (blue), and in the first coronal image (D), several liver artifacts can be seen at the distal portion of the lung ROI (red arrow). (E) In the transaxial view, the liver is seen within the lung ROI (blue) and a slight hazy/fuzziness can be seen on the left side of the image (red arrow), indicating diaphragm motion. The histogram (F) shows a second curve (0 to +100 HU) which is the liver.

3.4 Density differences in the normal lung vs diseased lung were detectable on the CBCT

Three rhesus macaques were infected intrabronchial with ~50 CFU of *M. tuberculosis* H37Rv-mCherry and followed for disease progression. The coronal and transaxial images of a single rhesus macaque on both scanners are shown in Fig.3. A normal macaque lung is shown (A and D) without any abnormalities. The red arrows point out vessels and the blue arrows point out airways. These are used as landmarks for analysis. The large white patches within the red box (B and E) are tubercular lesions. These are further blown up (C and F) and a vessel and airways are pointed out within these lesions.

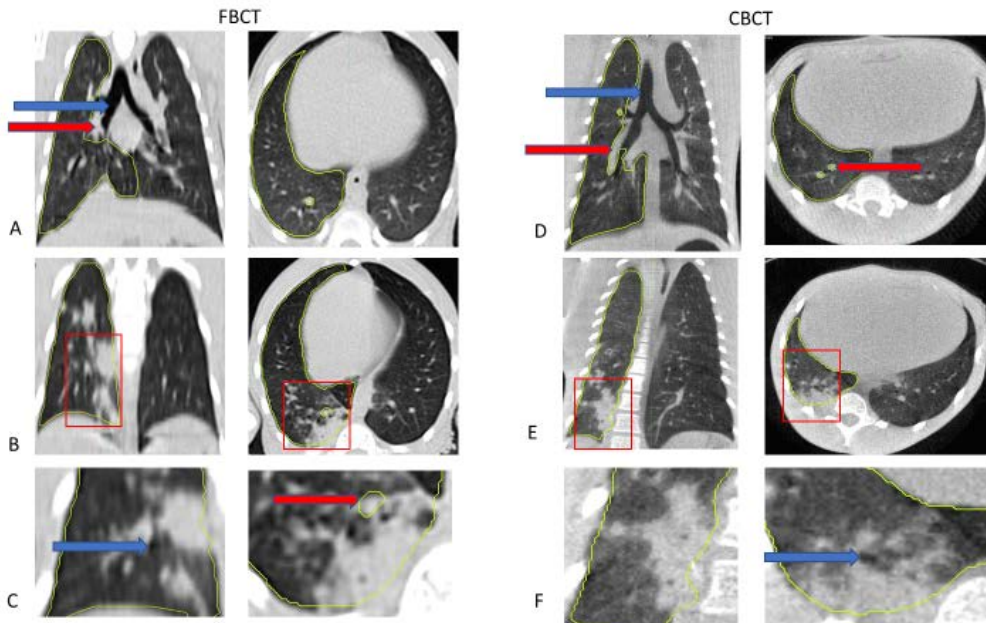


Figure 3 Representative images of normal lung and diseased lung as captured by the two scanners

Coronal and transaxial images of a single rhesus macaque as acquired on each of the scanners. A coronal and transaxial view of a naïve rhesus macaque taken on the FBCT (A) and CBCT (D). The lung has been outlined in yellow. No abnormalities seen. A coronal and transaxial view of the same rhesus macaque but at 10 weeks post infection depicts large white tubercular patches (red box) within the lung ROI of the FBCT (B) and CBCT (E). The red arrows depict vessels and the blue arrows depict airways.

3.5 Quantitative comparison of tubercular disease as captured by a CBCT and FBCT

Each rhesus monkey served as its own control. The normal lung HU bin was subtracted from the most diseased state. For the rest of the paper, we will focus on the disease range. These rhesus macaques were not significantly infected reflecting the small curve seen on the FBCT between -200 and +100 HU. The CBCT scanner showed a small curve from -300 to 0 HU. While no animal was sick, we were able to monitor the disease

progression using imaging tools. The normal volume (dashed lines) for primates DG1R and DGWZ are partially hidden by the disease volume (solid line) of DG1R.

The reconstruction method affects the detection of hardening disease as depicted in Figure 4. The FBCT identified more lung volume overall than the CBCT but was not as sensitive to the increase in HU density at the hardened disease (-500 to +200) as the CBCT. This is partially due to the CBCT collecting smaller pixels which generates a less blurry (greater spatial resolution) image. The phantom data (Table 3) showed a discrepancy in density ranges between the two scanners from the NEMA standards. These differences are seen in figure 4 with the FBCT detecting an increase in lung density around +50 HU and the CBCT detecting an increase in lung density at -100 HU.

TM2 week 8 (orange line) of figure 4A, shows a rather significant increase in disease volume compared to the other rhesus macaques. The other rhesus appeared to have volume in this same area.

The total voxel volume of the serial CT scans was summed by binning volumes spanning 10HU and graphed to determine the HU changes in the lung over the course of the infection, as defined in ¹⁸. The normal lung HU can be seen on the FBCT between the HU values of -950 to -600. This accounts for approximately 86% of the naïve lung at the 10HU binning. The CBCT recognizes normal lung tissue around -850 to -450 HU. This curve accounts for approximately 94% of the naïve lung at the 10HU binning. The peak heights are determined by a variety of factors including; extent of inflation during breath hold, physical size of the rhesus lung, and length of breath hold. Most notably, the peak around +50 HU in the FBCT and -100 HU in the CBCT captures the increase in lung

density as the granulomas form. The increase in abnormal lung density (> -500 HU) increased at different points during infection per rhesus.

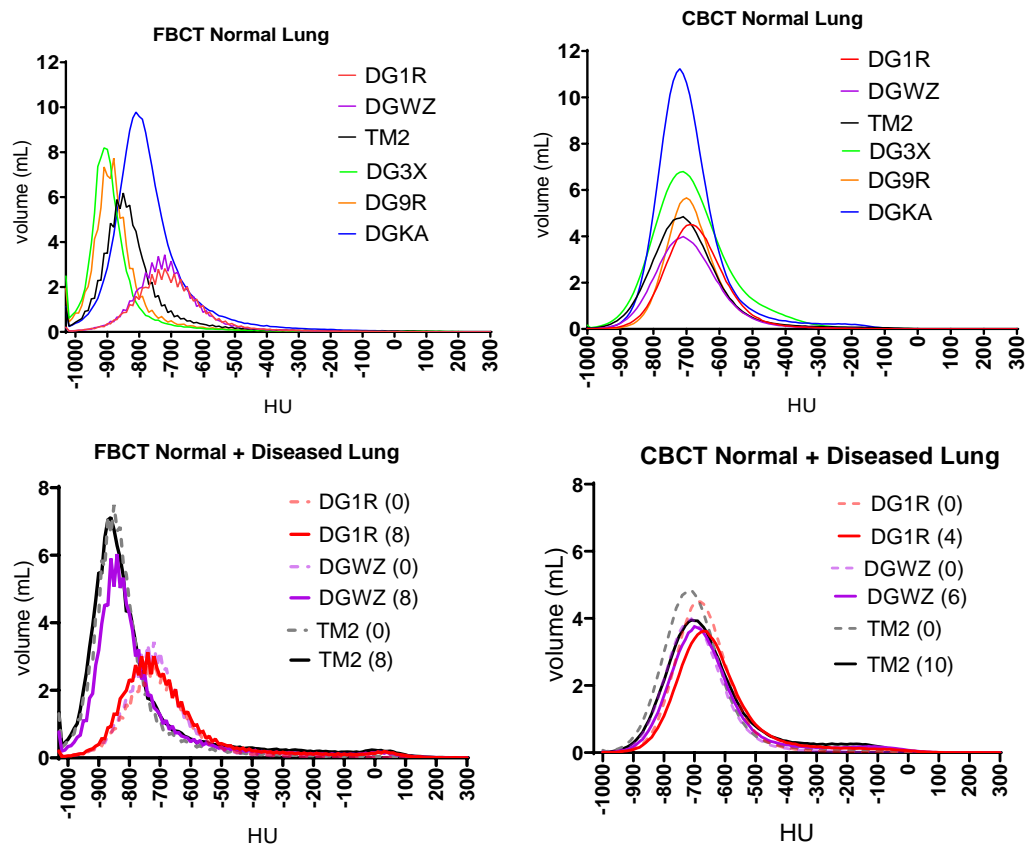


Figure 4 Normal and diseased lung profiles from images collected on the FBCT and CBCT

The normal lung tissue voxels have HU in the range -950 to -750 on the FBCT. This accounts for approximately 86% of the naïve lung voxels. The CBCT profiles normal lung tissue in the range of -850 to -500 HU. This curve accounts for approximately 94% of the naïve lung voxels. The small increase in HU (density) around 0 HU (FBCT) and -150 HU (CBCT) is where the scanner profiles change with the presence of tubercular disease.

3.6 Identifying disease over time between a FBCT and CBCT

We needed to establish defined disease ranges, so when experimental subjects are scanned on either CT, a known disease range can be incorporated into the analysis, as we work toward developing an automated analysis method.

To quantify these changes in abnormal lung density, we extracted the total three-dimensional lung volumes of the pre-infection scan and summing the volume occurring at each density in each scan. The HU distributions of the serial scans were plotted and examined to identify the density of diseased lung (the data from each animal is shown in figures 5A-F). In the naive adolescent rhesus macaque, tissue with a density greater than -500 HU accounts for less than 5% of the total lung volume, as defined by the marmoset methods from (Via, Weiner et al, 2013).

The total voxel volume of the serial CT scans was summed by binning volumes spanning 10 HU and graphed to visualize the HU changes in the lung over the course of the infection, as defined in ¹⁸. Most notably, the peak around +50 HU in the FBCT and -100 HU in the CBCT captures the increase in lung density as the granulomas form. The increase in abnormal lung density (> -500 HU) increased at different points during infection per rhesus. While their disease load was mild, TM2 can be seen at week 10 as having the highest disease load on both scanners, DGWZ has its highest disease load identified at week 6 on both scanners and DG1R showed a higher disease load at week 8 on the FBCT and week 4 on the CBCT. This discrepancy is most likely due to animal positioning on the scanner.

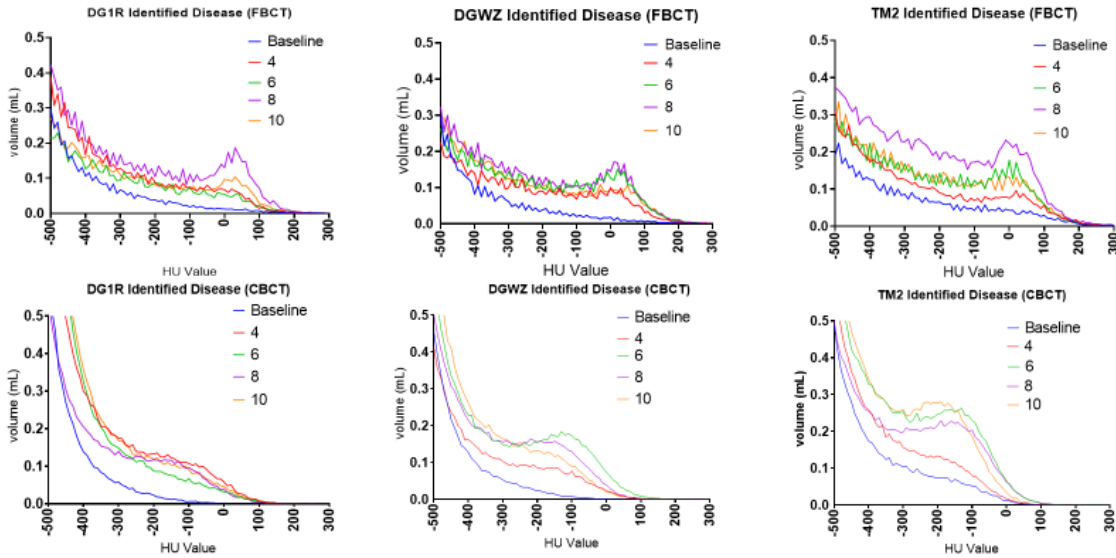


Figure 5 Visualizing changes in disease volume over time

Identifying disease over time between a FBCT (A-C) and CBCT (D-F). (A-C) Three different *M. tuberculosis* infected rhesus macaque were scanned on a FBCT over a 10-week period. The FBCT starts to identify a change in HU density around -497 HU with a peak difference from baseline around 0 to +50 HU. The CBCT started to distinguish a change in HU density around -497 HU with a peak difference from baseline around -200 to -100 HU.

3.7 Single Lesion Identification on FBCT using Established HU Ranges

We confirmed the FBCT HU density range from figure 5 by applying the -500 to +200 HU range to single Mtb lesions in a rhesus macaque (Figure 6, plates A-C) and a rabbit infected in another study (Figures 6, plates D-F). The dissemination of *M. tuberculosis* H37Rv-mCherry in the rhesus macaque did not yield any cavities 10 weeks post infection (Figure 6, plates A-C), but there were a plethora of lesions and the rabbit pictured had several cavities, which one is identified in figure 6 D-F.

The histograms C and F support this by identifying a higher percentage of voxels around the +50 HU value, which suggests a granuloma(s). This method confirms that the range lock of -500 to +200 identifies diseased lung tissue.

While the lesions in figure 6 are anatomically different, a significant peak is noticeable at +50HU, confirming the range lock of -500 to + 200 to be an appropriate range for diseased tissue. An ROI of a cavity (Figures 6 and 7 D-F) in a rabbit infected with *M. tuberculosis* HN878 was identified either during CT scans as lesions with centers approaching -1,000 HU (the density of air) or during dissection as lesions that contained air.

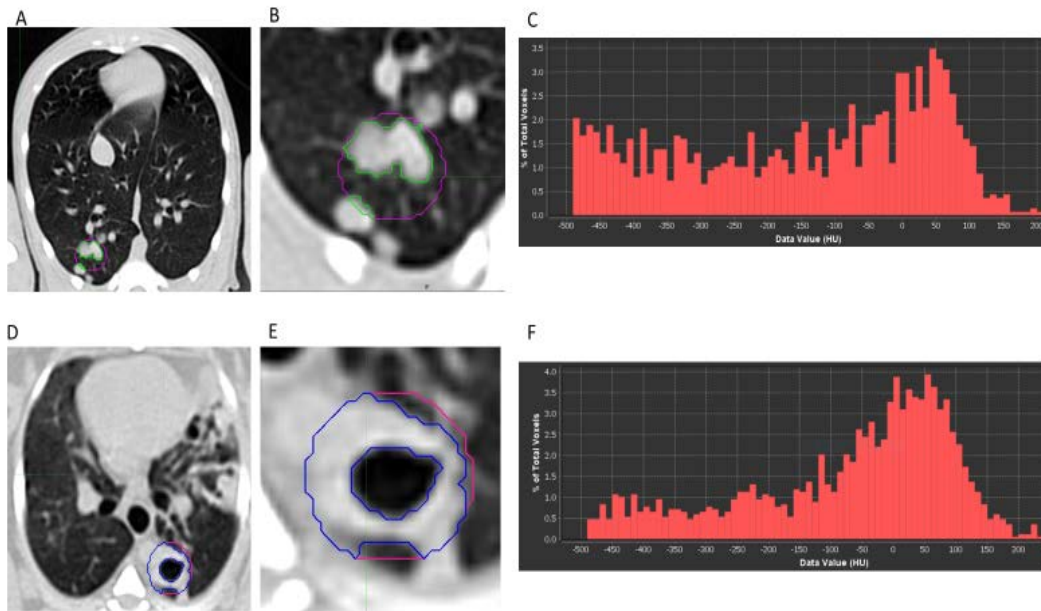


Figure 6 Single lesion identified on FBCT using established HU ranges

Confirmation of whole lung lesion analysis HU values identification by focusing in on specific lesions confirmed by necropsy. (A-C) Dissemination of *M. tuberculosis* in the rhesus macaque did not yield any cavities 10 weeks post infection but a plethora of hard and soft lesions. (D-F) Cavities as they appear in a rabbit approximately six months after infection with *M. tuberculosis* strain HN878. The original ~20mm ROI in B (purple) and E (pink) were further range locked using -500 to +200 HU, B (green) and E (blue). The histograms reflect the range locked ROI (green and blue) and confirm an increase in HU density around +50 HU identifying diseased lung.

3.8 Single Lesion Identified on a CBCT using established HU Ranges

We examined the same lesions in CT scans collected on the CBCT to confirm the disease range identified in the WLA of CBCT scans. Figure 7 (plates A-C) depict a cluster of lesions in the lung parenchyma and the HU density range of the voxels in the lesions within the ROI.

This analysis confirms that the range lock of -500 to +200 HU identifies diseased lung as shown in the corresponding histograms of figures 7C and 7F. While the lesions

below were anatomically different, a significant peak was noticeable at -100HU, confirming the range lock of -500 to + 200 to be an appropriate range for diseased tissue.

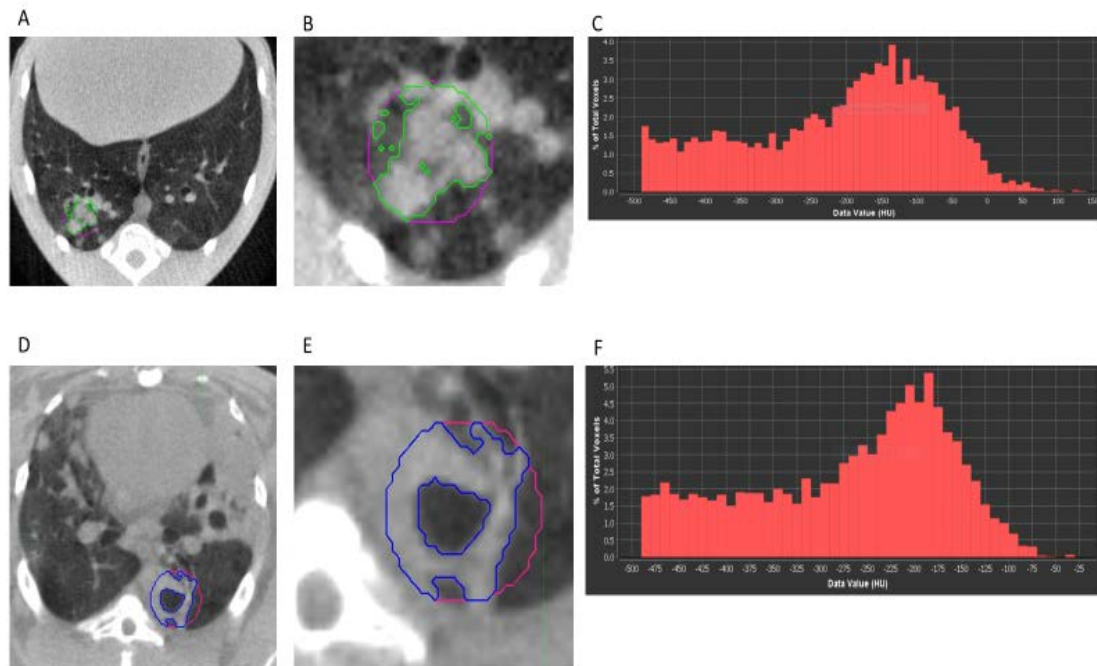


Figure 7 Single lesion identified on a CBCT using established HU ranges

Confirmation of whole lung lesion analysis HU values identification by focusing in on specific lesions confirmed by necropsy. The original ~20mm ROI in B (purple) and E (pink) were further range locked using -500 to +200 HU, B (green) and E (blue). The histograms reflect the range locked ROI (green and blue) and confirm an increase in HU density around -150 HU for the rhesus macaque (7C) and -175 HU for the rabbit (7F) identifying diseased lung.

3.9 Disease progression comparison between FBCT and CBCT on one rhesus macaque.

The progression of density changes of rhesus macaque, TM2, from baseline to week 10 can be seen in figure 8. The top row is the disease progression as represented on the FBCT and the bottom row on the CBCT. The lung ROI is not shown due to it masking some disease. These images are snapshots of each disease state. It does not illustrate complete disease volume as TM2 had disease that disseminated to the distal right lung lobes, not shown in the images. The red arrow tracts a TB lesion over time and a clear increase in the volume of diseased tissue in the whole lung was observed. Week 4 on the CBCT, the lesion being followed has yet to be seen with the possibility of the animal positioning obscuring it. This abnormal lung volume continued to increase from week 6 to week 8, as seen in figure 5. On the CBCT during week 8, the extreme distal portion of the thoracic cavity was not scanned, and part of the disease volume was not captured for this time point.

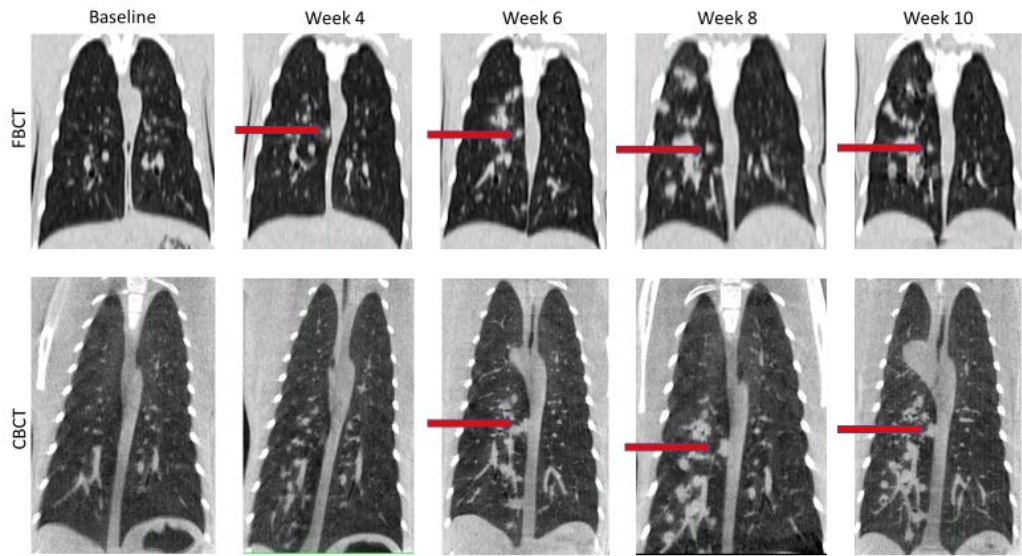


Figure 8 Disease progression/regression over 10 weeks on a FBCT and CBCT
Tubercular disease progression can be seen on both the FBCT (top) and CBCT (bottom). The red arrows tract an *Mtb* lesion over the course of the study. An overall increase in disease from baseline can be seen. These are snap shots, and do not depict all of the disease in the distal portion of the right lung.

3.10 Change in disease volume over time on CBCT vs FBCT imaging systems

The purpose of scanning our macaques during infection is two-fold: scanning provides us a snapshot of the extent of disease so that we can monitor their health and second it provides a quantitative measure of disease to judge the activity of chemical or immunological treatments we are evaluating. Using the method described in figure 5, we subtracted the baseline (or naïve) lung volume in the relevant range (-500 to +200 HU) from the lung volume in that range after 4,6,8, and 10 weeks of infection to compute the volume of disease over time (Figure 9).

Once the macaques reached 6 weeks post infection, the increase in disease volume began to level off in DG1R and DGWZ but continued to increase in TM2 on the FBCT. The disease volume for DG1R (blue line) is sporadic on both scanners. After reviewing the whole lung ROIs, the inflation of DG1R's lungs varied over each week, and the positioning of the animal was significantly different on the CBCT from the FBCT. The heart could be seen laying further into the right lung field, then left lung field, which decreased the overall lung volume. These positioning issues may have made the very minimal disease in DG1R difficult to quantify.

The disease volume at week 8 for TM2 (green line) on the CBCT is removed due to the distal portion of the lung not being captured during scanning, which resulted in insufficient quantification of the disease. The FBCT was not readjusted to fit this loss and illustrates TM2's most diseased week to be week 8. The amount of disease in the distal lung appears to progress considerably and what was excluded from the CBCT was not excluded from the FBCT, and a steady disease progression can be seen.

While these macaques were not significantly diseased (less than 10% of their right lung volume), we are able to monitor disease progression to detect resolving disease and could have detected dangerous disease progression if it had occurred.

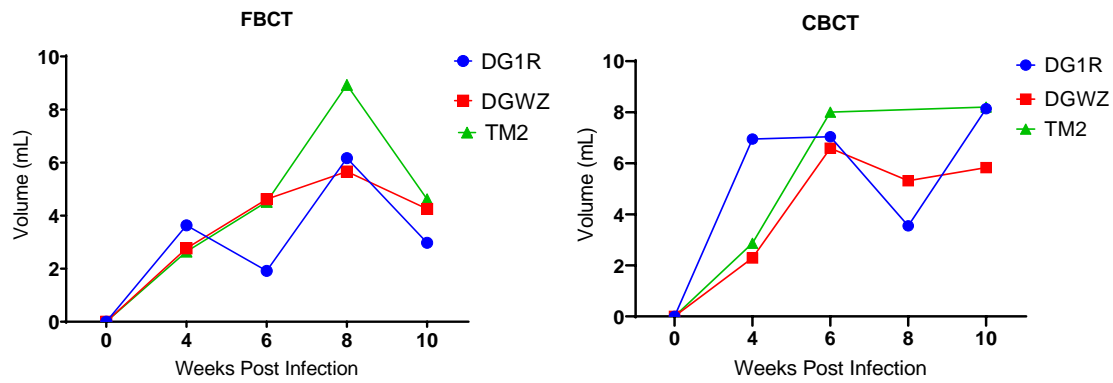


Figure 9 Change in disease volume over time on a FBCT vs CBCT

While none of the primates were extensively infected, TM2 showed the greatest increase in disease (green line), from baseline on the FBCT. The CBCT scan for TM2 at week 8 excluded the distal portion of the lungs, where there was disease and we were not able to accurately quantitate disease volume. TM2's FBCT lung ROI for week 8 was not readjusted and suggests week 8 as the most diseased week.

DISSCUSION

Although there are several animal models used in *M. tuberculosis* research, NHPs are the most closely related to humans, both genetically and with respect to *M. tuberculosis* infection outcome and pathology. Rhesus macaques are the most commonly used NHP species in TB research. Our goal for this study was to determine the hounsfield unit (HU) range of normal lung tissue and tubercular diseased lung tissue of the same rhesus macaque on repeat scans using two different manufacturers' scanners, a non-clinical cone beam computerized tomography scanner (CBCT) versus a clinical fan beam computerized tomography scanner (FBCT). These methods and disease ranges defined for the CBCT will be applied towards other model species used in the laboratory such as, marmosets and lagomorphs. While comparative studies have been done previously^{9,19}, the current study uses rhesus macaques to compare a clinical FBCT that has been used for multiple published studies^{18,20-22} to a new non-clinical CBCT recently purchased to provide a comprehensive and quantitative method for identifying tubercular lesion volume in the lung in future Mtb studies.

A low contrast phantom, similar to a Catphan® phantom, was used to determine the performance of the FBCT and CBCT. A Catphan® phantom is used for quality control of CT scanners to evaluate image quality and detect calibration decay of the scanner. In previous studies^{19,23}, guidelines were based on image quality parameters in axial scanners. In clinical practice, helical scanners are used primarily for their advantages in motion artifact reduction, decreased scan time and decreased effective radiation dose. A database,

like the ones published by the Medical Imaging and Technology Alliance (MITA), is necessary as a reference for researchers who use axial scanners on their non-clinical patients to determine the scanners performance as published by NEMA. NEMA testing represents the gold standard for acceptance testing. The HU values for the CBCT and the FBCT show an obvious discrepancy because of the beam types (Table 3).

Non-clinical scanners do not have a set of industrial standard ranges like clinical scanners that are used for disease diagnosis and have to meet FDA medical device standards and be calibrated to remain in compliance with various medical device oversite standards. For researchers using non-clinical scanners, the devices do not have to meet the same standards, nor are audits conducted to confirm that the device remains in compliance. Calibration and setting up standard protocols to confirm that the scanner continues to perform similarly year after year is up to the individual research group as defined by their application.

The data presented here show that non-clinical CBCT has a sharper image quality because of the smaller voxel size and lower radiation dose (Table 2), while the clinical FBCT has better contrast and less noise due to the beam style but subjects the patient to a higher dose of radiation. The sharper image or the ability to distinguish sharp edges between small objects that differ greatly in density (spatial resolution) is due to smaller voxel size which is the three-dimensional element of a pixel, the building block of the matrix and image.

Aside from image quality, the DLP volume was 14 times higher in the clinical FBCT than the non-clinical CBCT. This aspect is important to consider, given the patient

size. The lower CBCT radiation dose is due to a significantly weaker amperage, which is the number of x-rays produced during the exposure. The CBCT generated 820uA and the FBCT generated 5mA. The higher amperes are needed to penetrate larger patients or thicker dense structures like the skull.

Achieving consistent disease presentation in outbred animals can be challenging. The use of molecular imaging in the rhesus macaque provides for simple, serial quantitative assessments of disease progression where each animal provides its own baseline. The 3 rhesus macaques used for this study showed minimal disease load, but the increase in HU densities was seen at week 4 as demonstrated in figure 5. These increases in HU density were confirmed on individual lesions (figures 6 and 7) from a rhesus macaque and a previously published rabbit.

The cavity structure shown in Figures 6 and 7 D-F, included an extensive central necrotic zone surrounded by a layer of intact macrophages, lymphocytes, and fibroblasts contained within an outer fibrotic wall ²². A soft tissue lesion, in a rabbit, is considered to have densities that range from -300 to -100 HU but can be higher for calcified areas. Therefore, the lung volumes were divided into three ranges: high density for soft lesions (-125 to 175), medium density for hard lesions (-625 to -225) and low density for normal lung (-1,024 to -725) (²². These ranges still need to be identified in other species. The classification (hard vs soft) was not performed in this study, but will be needed in future studies, along with extensive pathology to identify the evolution of individual lesion densities.

The quantitative analysis of the image quality study comparing CBCT and FBCT brought forth many results. The FBCT system appears to have lower artifact presence and a greater ability to discriminate low contrast objects compared to CBCT which appears to have a better spatial resolution due to the large quantity of smaller voxels. CBCT systems are intrinsically more prone to scattering, beam hardening, and artifacts ⁹. This CBCT showed relative supremacy in the spatial resolution readings compared to FBCT models used. Which implies that CBCT has a greater ability to distinguish small spatial variations, though it's important to reiterate that these values can vary greatly depending on imaging protocol settings. These image quality measurements were taken using a rhesus macaque model to provide a numerical quantitation of diseased tissue densities vs non-diseased tissue densities.

The positioning of the primates on the scanner bed is essential to capturing not only the disease as a whole but being able to track individual lesions. DG1R, was often improperly positioned during scanning on the CBCT. This led to: incorrect inflation of the lungs, from one lung being more compressed/inflated than the other, shifting of the heart further into a lung field which alters the lung ROI, and compression of major bronchial airways and lesions which makes lesion identification difficult to impossible because they are not in the same field of view as previous scans or are completely obscured.

To quantify abnormal lung density, we extracted the total three-dimensional lung volumes to the pre-infection scan and summing the volume occurring at each density in each scan. The HU distributions of the serial scans were plotted. In the naive adolescent rhesus, the increase in abnormal lung density (> -500 HU) increased at different points

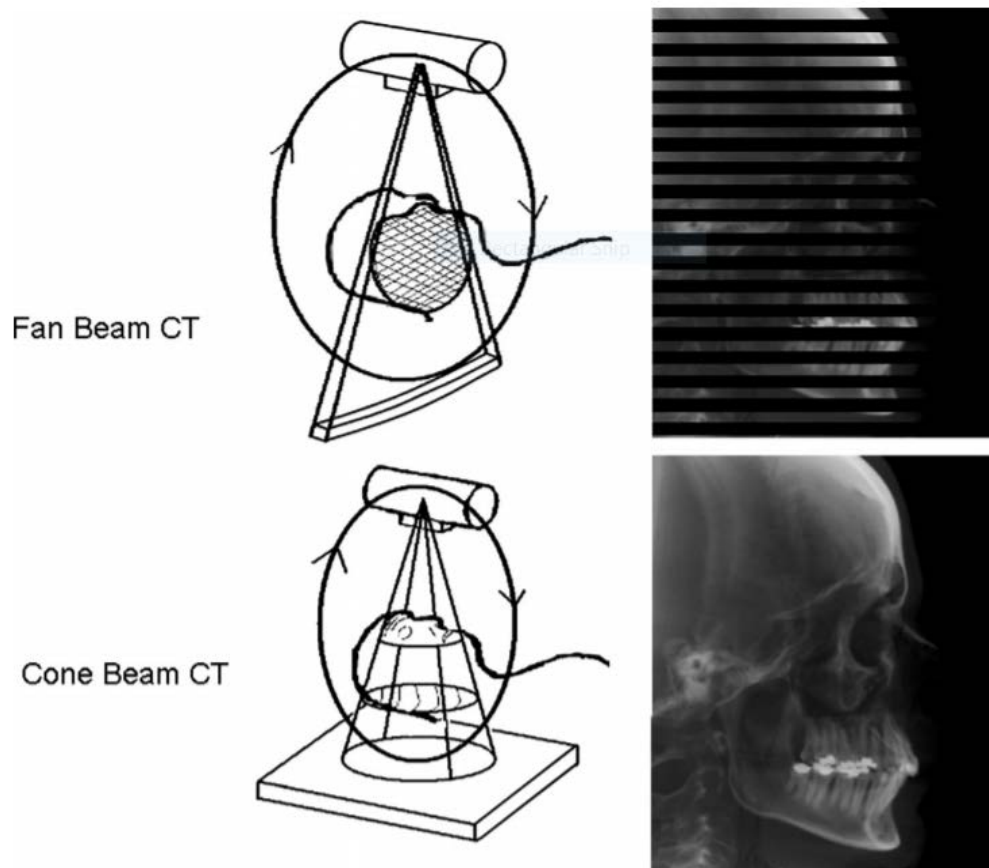
during infection per rhesus. While their disease load was mild, TM2 and DGWZ correlated has having their highest disease load match on both scanners, week 10 and week 6, respectively. DG1R showed a discrepancy in highest disease load between the scanners. This is most likely due to improper positioning which led to obscuring some disease and lung volume differences from improper inflation or heart placement, as mentioned above.

There are three major limitations in this study that could be addressed in future research. First, this study included a small sample size which made it difficult to find significant relationships from the data, so statistical tests ensure a representative distribution of the population. Second, there is limited research on the comparison of a FBCT and CBCT using the rhesus macaque model. Further development of in vivo research will need to be performed to effectively compare a FBCT to a CBCT in the research field. Third, the scant amount of disease that developed in the right lung during this study, limited the scope of the analysis. Allowing more time for the disease to progress is needed in future studies.

CONCLUSION

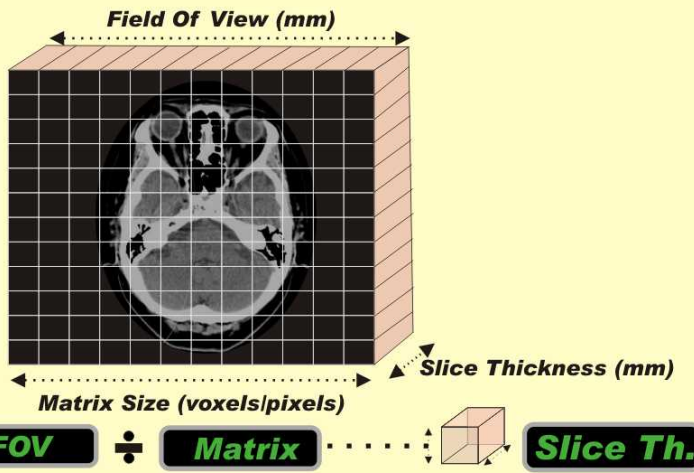
This rhesus macaque study shows the importance of keeping the patient on the same scanner for the duration of the study for quantitative purposes. Discrepancies are seen in the image quality, DLP measurements and animal positioning. The HU density where disease is first established on the FBCT and CBCT is -497HU and diminishes to negligible HU values around +200 HU. This suggests that a range lock of -500 to +200 HU can be applied to identify potential diseased TB lung areas on the rhesus macaque. Further studies are needed to identify hard and soft areas of tubercular lesions. This study can be applied to determine the appropriate quantitative HU density range of other species tubercular disease formation.

APPENDIX



Supplementary Image 1 Comparison of fan beam and cone beam computed tomography imaging geometry²⁴. The FBCT used in this study is an 8-slice CT.

CT Slice Divided into Matrix of Voxels



Voxel Size Controlled By

Sprawls

Supplementary Image 2. Voxel formation during the reconstruction phase²⁵.

REFERENCES

- 1 Ahn, B. C. Use of Nuclear Medicine Technology for Clinical Molecular Imaging: a Message from the Associate Editor. *Nucl Med Mol Imaging* 50, 183-184, doi:10.1007/s13139-016-0413-1 (2016).
- 2 Khalil, M. M., Tremoleda, J. L., Bayomy, T. B. & Gsell, W. Molecular SPECT Imaging: An Overview. *J International Journal of Molecular Imaging* 2011, doi:10.1155/2011/796025 (2011).
- 3 Pichler, B. J., Wehrli, H. F., Kolb, A. & Judenhofer, M. S. Positron emission tomography/magnetic resonance imaging: the next generation of multimodality imaging? *Semin Nucl Med* 38, 199-208, doi:10.1053/j.semnuclmed.2008.02.001 (2008).
- 4 Seeram, E. Computed Tomography: A Technical Review. *Radiologic technology* 89, 279-302 (2018).
- 5 Jarritt, P. H., Carson, K. J., Hounsell, A. R. & Visvikis, D. The role of PET/CT scanning in radiotherapy planning. *The British journal of radiology* 79 Spec No 1, S27-35, doi:10.1259/bjr/35628509 (2006).
- 6 Qiu, D. & Seeram, E. Does iterative reconstruction improve image quality and reduce dose in computed tomography. *Radiol Open J* 1, 42-54, doi:10.17140/ROJ-1-108 (2016).
- 7 Scarfe, W. C. & Farman, A. G. What is cone-beam CT and how does it work? *Dent Clin North Am* 52, 707-730, doi:10.1016/j.cden.2008.05.005 (2008).
- 8 Elstrøm, U. V., Muren, L. P., Petersen, J. B. B. & Grau, C. Evaluation of image quality for different kV cone-beam CT acquisition and reconstruction methods in the head and neck region. *Acta Oncologica* 50, 908-917, doi:10.3109/0284186X.2011.590525 (2011).
- 9 Lechuga, L. & Weidlich, G. A. Cone Beam CT vs. Fan Beam CT: A Comparison of Image Quality and Dose Delivered Between Two Differing CT Imaging Modalities. *Cureus* 8, e778, doi:10.7759/cureus.778 (2016).
- 10 Antunovic, L., Rodari, M., Rossi, P. & Chiti, A. Standardization and quantification in PET/CT imaging: tracers beyond FDG. *PET Clin* 9, 259-266, doi:10.1016/j.cpet.2014.03.002 (2014).
- 11 Lauridsen, H. et al. Inside out: modern imaging techniques to reveal animal anatomy. *PloS one* 6, e17879, doi:10.1371/journal.pone.0017879 (2011).
- 12 Walter, T. et al. Visualization of image data from cells to organisms. *Nat Methods* 7, S26-41, doi:10.1038/nmeth.1431 (2010).
- 13 Langermans, J. A. et al. Divergent effect of bacillus Calmette-Guerin (BCG) vaccination on Mycobacterium tuberculosis infection in highly related macaque species: implications for primate models in tuberculosis vaccine research. *Proceedings of the National Academy of Sciences of the United States of America* 98, 11497-11502, doi:10.1073/pnas.201404898 (2001).
- 14 Sharpe, S. A. et al. Determination of lesion volume by MRI and stereology in a macaque model of tuberculosis. *Tuberculosis (Edinburgh, Scotland)* 89, 405-416, doi:10.1016/j.tube.2009.09.002 (2009).

- 15 Sharpe, S. A. *et al.* Establishment of an aerosol challenge model of tuberculosis in rhesus macaques and an evaluation of endpoints for vaccine testing. *Clinical and vaccine immunology : CVI* 17, 1170-1182, doi:10.1128/cvi.00079-10 (2010).
- 16 McCollough, C. H. *et al.* CT dose index and patient dose: they are not the same thing. *Radiology* 259, 311-316, doi:10.1148/radiol.11101800 (2011).
- 17 Christian, P. E. & Waterstram-Rich, K. M. *Nuclear medicine and PET/CT: Technology and Techniques*. 7th edn, (Elsevier Mosby, 2012).
- 18 Via, L. E. *et al.* Differential Virulence and Disease Progression following Mycobacterium tuberculosis Complex Infection of the Common Marmoset. *Infection and Immunity* 81, 2909-2919, doi:10.1128/IAI.00632-13 (2013).
- 19 Ratliff, S. T. Webb's Physics of Medical Imaging, Second Edition. 40, 097301, doi:10.1118/1.4818282 (2013).
- 20 Maiello, P. *et al.* Rhesus Macaques Are More Susceptible to Progressive Tuberculosis than Cynomolgus Macaques: a Quantitative Comparison. *Infect Immun* 86, doi:10.1128/iai.00505-17 (2018).
- 21 Via, L. E. *et al.* A Sterilizing Tuberculosis Treatment Regimen Is Associated with Faster Clearance of Bacteria in Cavitary Lesions in Marmosets. *Antimicrobial Agents and Chemotherapy* 59, 4181-4189, doi:10.1128/AAC.00115-15 (2015).
- 22 Via, L. E. *et al.* Infection dynamics and response to chemotherapy in a rabbit model of tuberculosis using [¹⁸F] 2-fluoro-deoxy-D-glucose positron emission tomography and computed tomography. *Antimicrob Agents Chemother* 56, 4391-4402, doi:10.1128/AAC.00531-12 (2012).
- 23 Husby, E., Svendsen, E. D., Andersen, H. K. & Martinsen, A. C. T. 100 days with scans of the same Catphan phantom on the same CT scanner. *Journal of applied clinical medical physics* 18, 224-231, doi:10.1002/acm2.12186 (2017).
- 24 Farman, A. G. & Scarfe, W. C. The Basics of Maxillofacial Cone Beam Computed Tomography. *Seminars in Orthodontics* 15, 2-13, doi:10.1053/j.sodo.2008.09.001 (2009).
- 25 Sprawls, P., Jr. *Physical Principles of Medical Imaging*. Second edn, (Medical Physics Publishing, 1995).

BIOGRAPHY

Michelle Sutphin graduated from Fauquier High School, Warrenton, Virginia, in 2003. She received her Bachelor of Science in Zoology from Palm Beach Atlantic University in 2007. She received her Associates of Veterinary Technology from Penn Foster in 2015 and is licensed to practice as a veterinary technician in Virginia and Maryland. She is employed as a Research Support Specialist/PET/CT Technologist at the National Institutes of Health for the Tuberculosis Research Section and the Tuberculosis Imaging Program of NIAID in Montgomery County for five years and received her Master of Science in Biology from George Mason University in 2019.